Phase Adjustment and ISAR Imaging of Maneuvering Targets With Sparse Apertures

LEI ZHANG, Member, IEEE

JIA DUAN
Xidian University
China

ZHI-JUN QIAO, Member, IEEE
University of Texas–Pan American

MENG-DAO XING, Member, IEEE

ZHENG BAO, Life Senior Member, IEEE
Xidian University
China

A multifunctional radar system can only acquire limited and discontinuous wideband pulses, which form sparse aperture (SA) observations of a target. To carry out radar activities (detection, tracking, and imaging) simultaneously for multiple targets, inverse synthetic aperture radar (ISAR) imaging exploiting these SA data is essential for multifunctional radar. In this paper, we study the phase adjustment and full-aperture (FA) reconstruction for SA-ISAR imaging of maneuvering targets. A modified eigenvector-based autofocus approach is proposed to correct phase errors within SA measurements of maneuvering targets. After phase correction, the FA data are reconstructed from SA measurements via sparse representation under a redundant chirp–Fourier dictionary. An efficient algorithm is developed to solve the sparse decomposition optimization, and ISAR images of the maneuvering target are obtained by adaptive joint time-frequency imaging approaches with the reconstructed data. Both simulated and real data sets are used to confirm the effectiveness of the proposed methods.

Manuscript received February 23, 2013; revised July 21, 2013; released for publication November 5, 2013.

DOI. No. 10.1109/TAES.2013.130115.

Refereeing of this contribution was handled by C. Baker.

This work was supported by the Fundamental Research Funds for the Central Universities under grant K5051302001 and K5051302078 and by the National Natural Science Foundation of China under Grant 61301280 and JJ0200122201.

Authors' addresses: Lei Zhang, Jia Duan, Meng-dao Xing, and Zheng Bao, Xidian University, National Lab of Radar Signal Processing, Taibai Road Num.2, Xi'an, Shann'xi 710071 China, E-mail: (zhanglei_0330@126.com); Zhi-jun Qiao, Department of Mathematics, University of Texas–Pan American, Edinburg, TX.

I. INTRODUCTION

Recent development in active phased array radar techniques has enabled modern radar system to integrate multiple functions without increasing system complexity [1]. In the multifunctional radar system, the source of system time and power is optimally allocated for different tasks, such as searching, multitarget tracking, and imaging. Radar activities are usually executed simultaneously by using a periodic or nonperiodic time-sharing mechanism. In spite of great benefits, new challenges arise through use of these time-sharing mechanisms. For inverse synthetic aperture radar (ISAR) imaging acquiring a long and continuous wideband observation of a target is difficult because of its contention with other important tasks. For example, the radar beam needs to switch from among several directions to track multiple targets continuously and simultaneously. As a result, for each target, the wideband observation for ISAR imaging is limited and sparsely recorded. Multisourced interferences may also contaminate some portions of acquired data, yielding gaps. These incomplete data form sparse aperture (SA) measurements. Moreover, the SA measurements would be introduced in a netted radar system with multiple angular diversities [2, 3]. High-resolution ISAR imaging with limited SA measurements is essential to increase the flexibility and robustness of multifunctional radar.

Recent studies show the suppression of discontinuous aperture effects on radar imagery, and many approaches have been proposed. Generally speaking, recently developed approaches may be sorted into four kinds: 1) Modern spectral estimate algorithms can effectively handle SA data. They estimate the complex-value amplitude and frequency of each sinusoidal signal component from gapped data by interpolating missing samples under certain constraints. Gapped-data amplitude and phase estimation [4, 5] algorithms are two of those representative approaches. 2) Prediction-based interpolation and extrapolation algorithms can solve the missing data problem in some situations where the available data are fitted into a linear prediction model. The missing data are recovered by the model coefficients and available observations [6–8]. 3) CLEAN techniques [9, 10] treat image formation from SA data as a deconvolution procedure. They estimate and subtract the main lobes of the strong scattering center responses iteratively until reaching convergence, which suppresses the high-gating lobes from missing data, to a certain degree. 4) Full-resolution imaging with SA can be converted into an optimization problem of sparse signal reconstruction, where the sparsity priority of the target scattering field is exploited to reconstruct the missing data [11–13]. Generally speaking, almost all currently existing methods for SA imaging deal with target echoes as multicomponent complex sinusoidal signals. For ISAR imaging, the sinusoidal signal assumption is only suitable for expressing the echo from a stable moving target within a relatively short coherent processing interval (CPI). ISAR

targets, such as flying planes and vessels on the sea, are usually noncooperative, and considerable maneuvering is involved in their motion, yielding time-varying Doppler modulation in the echoed signal. To image the maneuvering target, signal components are modeled as chirps or high-order frequency-modulated signals [14–19]. As a result, the assumption prevents current approaches from handling SA imaging of maneuvering targets. On the other hand, because of missing data within SA collections, current imaging approaches for a maneuvering target developed on the full-aperture (FA) data model, such as adaptive joint time-frequency analysis (AJTFA) [20–22], also fail to achieve ISAR images of high quality. To our knowledge, there is not yet a straightforward approach capable of accomplishing the task of high-resolution SA-ISAR imaging of maneuvering targets, which motivates our work reported in this paper.

Motion error is one of the most challenging problems in SA-ISAR imaging of maneuvering targets. Together with translational motion, severe vibration of the target or radar platform could induce significant high-frequency motion error in the received signal. The conventional motion compensation procedure for FA-ISAR data is composed of two independent steps: range alignment and phase adjustment [20]. Range alignment is the correction of range migration between different pulses. After that, phase adjustment is necessary to remove the phase error, which is usually viewed as autofocus processing. As one knows, some range alignment approaches are applicable to SA-ISAR data, such as the minimum entropy–based method [23]. However, phase adjustment for SA-ISAR data is difficult when using straightforward autofocus methods. Autofocus approaches inherently imply that the focused image and the range-compressed phase history constitute a pair of Fourier transforms. This assumption is an intrinsic basis of conventional phase adjustment approaches, such as [24–27]. However, this assumption fails in SA-ISAR imaging of maneuvering targets because of missing samples and the target movement, resulting in failure of most autofocus methods in SA cases. As an exception, eigenvector-based autofocus has been shown to be applicable in SA-ISAR imaging of stable targets [23]. Nevertheless, its performance dramatically degrades in SA-ISAR imaging of maneuvering targets because the maneuvering characteristics are not taken into account. Recently, some novel sparsity-driven methods [28–30] have also been proposed for phase correction in ISAR imaging with sparsely sampled data. These approaches usually convert the joint image formation and phase correction with incomplete measurements into an optimization problem of sparse representation, and the phase error is overcome in imaging processing in an iterative manner. Solving the optimization problem usually involves a large computation load, which may be an important obstacle in some real-time scenarios.

In this paper, we investigate robust and precise SA-ISAR imaging of maneuvering targets and mainly focus on phase adjustment and FA signal reconstruction. Based on the SA-chirp model, we develop an improved eigenvector autofocus method that precisely corrects the phase error in SA data of maneuvering targets. In our method, range cells containing dominant scatterers are selected to estimate the phase error in an iterative manner. Within the iteration, the first- and second-order phase terms of these dominant range cells are adaptively removed before the coherence matrix calculation for eigenvector autofocus processing; therefore, the negative effect from time-varying Doppler on phase error estimation is eliminated. The second method lies in FA reconstruction of missing data by sparse representation. Because the major energy of the target scattering field is contributed by a small number of scattering centers, the signal components of the received data are very limited. Under a redundant SA chirp–Fourier basis, the signal of each range cell can be represented sparsely, which means that the coefficients of the signal are sparse. FA data can be optimally reconstructed from SA data by solving an l_1-norm optimization problem. The l_1-norm optimization for sparse signal reconstruction is usually concerned in compressive sensing theory [31–33]. In this paper, an orthogonal matched-pursuit (OMP) algorithm is implemented to solve the optimization of FA data reconstruction under the SA chirp–Fourier basis. By adopting the recovered data, straightforward conventional rotation compensation can be applied, and range-instantaneous Doppler (RID) images of maneuvering targets are obtained by AJTFA approaches. Both the proposed phase adjustment and FA signal recovery methods are extended so that migration through range cells (MTRC) induced by target rotational motion is not nominal or to be neglected. Simulated and real data sets are utilized to confirm the effectiveness of the proposed methods in dealing with SA-ISAR imaging of maneuvering targets. Comparisons are also provided to show the improvement of the modified autofocus method.

The paper is organized as follows. In Section II, the SA-ISAR signal model for maneuvering targets is briefly introduced. In Section III, we present the improved eigenvector autofocus method. This section also formulates the optimization for FA data reconstruction in the framework of sparse representation, and extensions to MTRC cases are discussed in detail. Section IV provides numerical results to show the effectiveness and advantages of the proposed methods. Finally, some conclusions are summarized in the last section.

II. SA-ISAR SIGNAL MODEL FOR MANEUVERING TARGETS

In this section, we first introduce the ISAR geometry and signal models for maneuvering targets with three-dimensional rotation. Based on the ISAR geometry, the SA-ISAR signal model with phase error subsequently is developed.

Assuming the translational motion is corrected, the ISAR geometry of a maneuvering target is represented by

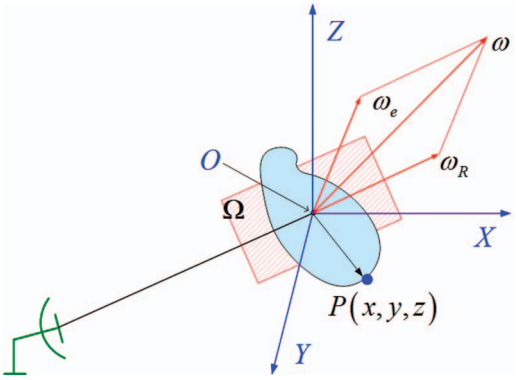

Fig. 1. ISAR geometry of maneuvering targets.

Fig. 1 [15]. $\boldsymbol{XYZ}$ defines a Cartesian coordinate with the rotating center of the target. The imaging plane $\boldsymbol{\Omega}$ is determined by vectors $\boldsymbol{\omega}$ and $\boldsymbol{R} = [x_R, y_R, z_R]^T$ ($\sqrt{x_R^2 + y_R^2 + z_R^2} = 1$), which represent the unit vectors of the angular velocity of the target and the unit vector along the radar line of sight, respectively. Without loss of generality, $\boldsymbol{\omega}$ can be decomposed into $\boldsymbol{\omega}_e$ and $\boldsymbol{\omega}_R$, which correspond to the components perpendicular and parallel to $\boldsymbol{R}$, respectively. Rotation from $\boldsymbol{\omega}_R$ does not cause radial motion or Doppler modulation in the echoed signal, whereas rotation from $\boldsymbol{\omega}_e$ contributes all Doppler modulation with respect to the synthetic aperture. Therefore, $\boldsymbol{\omega}_e$ is defined as the effective rotation. For the convenience of the following derivation, we write the effective rotational velocity as $\boldsymbol{\omega}_e = \left[\omega_{ex}, \omega_{ey}, \omega_{ez}\right]^T$. The symbol $\boldsymbol{O}$ stands for the origin of the coordinate system, which is actually the rotation center of the target. Let $\boldsymbol{P}$ be a scattering center with coordinate (x, y, z). For a maneuvering target, during the observation interval, its effective rotation is generally nonuniform, which means both the magnitude and direction of $\boldsymbol{\omega}_e$ may be time variant. The time variance of $\boldsymbol{\omega}_e$ for the maneuvering target can be expressed by the first-order approximation

$$\begin{cases} \omega_{ex} \approx \omega_{x0} + \alpha_x t_m \\ \omega_{ey} \approx \omega_{y0} + \alpha_y t_m \\ \omega_{ez} \approx \omega_{z0} + \alpha_z t_m \end{cases}, \tag{1}$$

where $\boldsymbol{\omega}_0 = \left[\omega_{x0}, \omega_{y0}, \omega_{z0}\right]^T$ is the starting rotational velocity, $\boldsymbol{\alpha} = \left[\alpha_x, \alpha_y, \alpha_z\right]^T$ is the vector of rotational acceleration, and t_m denotes the slow time. In this maneuvering target model, the effective rotation velocity is time varying, which is the main difference between maneuvering targets and stable ones. Assuming the radar transmits a signal with chirp waveform

$$s_T(\tau) = \text{rect}\left(\frac{\tau}{T_p}\right) \cdot \exp\left(j\pi\gamma\tau^2\right), \tag{2}$$

where τ denotes fast time, T_p is the pulse duration, and γ is the chirp rate, after dechirping-on-receive and residue video phase compensation [15], we have the received signal as

$$\begin{aligned} s_p(\tau, t_m) = \delta_p \cdot \text{rect}&\left[\tau - \frac{2R_p(t_m; x, y, z)}{c}\right] \\ &\cdot \exp\left[-j\frac{4\pi}{c}\gamma\left(\tau - 2R_{\text{ref}}(t_m)/c\right)\Delta R_p(t_m)\right] \\ &\cdot \exp\left[-j\frac{4\pi}{\lambda}\Delta R_p(t_m)\right], \end{aligned} \tag{3}$$

where δ_p stands for the scattering coefficient, c is light speed, λ is the wavelength, and $R_{\text{ref}}(t_m)$ is the reference range at t_m. The instantaneous range difference $\Delta R_p(t_m) = R_p(t_m) - R_{ref}(t_m)$ corresponds to $\boldsymbol{r}_p \bullet \boldsymbol{R}$. By applying the Fourier transform (FT) with respect to τ and neglecting the constants, we have the range-compressed signal expression

$$\begin{aligned} s_p(r, t_m) = \delta_p \cdot \text{sinc}&\left[\frac{2\gamma T_p}{c}\left(r - \Delta R_p(t_m)\right)\right] \\ &\cdot \exp\left[-j\frac{4\pi}{\lambda}\Delta R_p(t_m)\right]. \end{aligned} \tag{4}$$

According to the 3D rotational model in Fig. 1, the radial range induced by the effective rotation can be expressed by

$$\Delta R_p(t_m) = \int_{t_0}^{t_m} \left(\boldsymbol{\omega}_e \times \boldsymbol{r}_p\right) \bullet \boldsymbol{R} dt. \tag{5}$$

Substituting (1) into (5), we have

$$\begin{aligned} \Delta R_p(t_m) &= \int_{t_0}^{t_m} \left[\boldsymbol{\omega}_0 \bullet \boldsymbol{r} + (\boldsymbol{\alpha} \bullet \boldsymbol{r})\, t_m\right] dt_m \\ &= (\boldsymbol{\omega}_0 \bullet \boldsymbol{r})\, t_m + \frac{1}{2}(\boldsymbol{\alpha} \bullet \boldsymbol{r})\, t_m^2 \\ &= a_p t_m + \frac{1}{2} b_p t_m^2 + \Delta r_p(t_0), \end{aligned} \tag{6}$$

where $a_p = \boldsymbol{\omega}_0 \bullet \boldsymbol{r}$, $b_p = \boldsymbol{\alpha} \bullet \boldsymbol{r}$, $\boldsymbol{r} = [(yz_R - zy_R), (zx_R - xz_R), (xy_R - yx_R)]^T$, and $\Delta r_p(t_0)$ is the range of the scattering center at time t_0. Symbol "$\bullet$" denotes the dot multiplication of vectors. The orientation of $\boldsymbol{\omega}_e$ is changing during CPI, leading to fluctuation of the image plane. The rotational motion of the target is not known a priori. As a result, conventional range-Doppler (RD) imaging fails to deal with maneuvering targets. To handle the problem of a time-varying image plane, adaptive time–frequency representations are usually applied to achieve a sequence of target scattering projections on the instantaneous Doppler planes, which forms RID images.

For clarity of the autofocus and FA reconstruction approaches, we first assume that the MTRC induced by rotation can be neglected. Extensions to MTRC cases will be discussed in the next section in detail. By substituting (6) into (4), we have

$$\begin{aligned} s_p(r, t_m) \approx \delta_p \cdot \text{sinc}&\left[\frac{2B}{c}\left(r - \Delta r_p(t_0)\right)\right] \\ &\cdot \exp\left[-j2\pi\left(\theta_p + f_p t_m + \frac{1}{2}\gamma_p t_m^2\right)\right], \end{aligned} \tag{7}$$

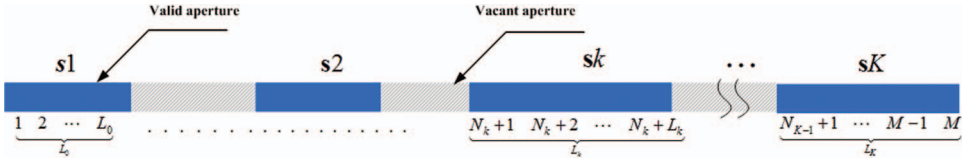

Fig. 2. SA-ISAR signal geometry.

where $\theta_p = \frac{2\Delta r_p(t_0)}{\lambda}$, $f_p = \frac{2a_p}{\lambda}$, and $\gamma_p = \frac{2b_p}{\lambda}$ represent the phase, Doppler frequency, and chirp rate, respectively.

In the above signal model, we assume that the translational motion is precisely compensated by range alignment and phase adjustment. Despite the missing pulse, the range alignment approaches in [23, 34, 35] are applicable. However, most of the autofocus approaches lose their efficacy in SA cases, because the vacant apertures break the FT relationship between the range-compressed data and the RD image. To complement the real SA-ISAR case, the residual phase error must be taken into account. A certain range cell after range compression is given by

$$s(t_m) = \sum_{p=1}^{P} s_p(t_m) \cdot \exp[-j \cdot \phi(t_m)]. \tag{8}$$

We assume that the range cell contains P scattering centers, and the signal component of the pth scattering center is still denoted by $s_p(t_m) = \delta'_p \cdot \exp\left[-j2\pi\left(f_p t_m + \frac{1}{2}\gamma_p t_m^2\right)\right]$. In (8), $\phi(t_m)$ represents the multisource phase error at t_m. For our convenience, we express the signal in the discrete form

$$\boldsymbol{s}(m) = \sum_{p=1}^{P} \mathbf{s}_p(m) \cdot \exp[-j \cdot \boldsymbol{\phi}(m)] \quad 1 \le m \le M, \tag{9}$$

where the FA data are assumed to contain a total of M pulses. $\boldsymbol{\phi}$ is an M-dimensional vector representing the phase error. Therefore, the signal of the pth scattering center can be rewritten as

$$\boldsymbol{s}_p(m) = \delta'_p \cdot \exp\left[-j2\pi\left(f_p m\Delta T + \frac{1}{2}\gamma_p m^2 \Delta T^2\right)\right] \quad 1 \le m \le M. \tag{10}$$

In the above context, we first introduce the signal model for maneuvering targets. Then, we extend it to the SA-ISAR cases. Because we consider that ISAR systems observe multiple moving targets simultaneously, radar illumination has to switch from one target to another very frequently, which leads to SA data for each target. Let the range cell be denoted still by the vector $\boldsymbol{s}$. We assume K SAs for a target consisting of a long aperture. Fig. 2 shows the geometry of apertures. The FA data should contain M pulses with an index from 1 to M. Suppose that the kth SA consists of L_k pulses (whose index ranges from $N_k + 1$ to $N_k + L_k$) represented by $\bar{\boldsymbol{I}}_k = [N_k + 1 \quad \cdots \quad N_k + L_k]^T_{L_k \times 1}$. Then, the vector corresponding to the kth SA is given by

$$\boldsymbol{s}k = \left[s(N_k+1) \quad s(N_k+2) \quad \cdots \quad s(N_k+L_k)\right]^T_{L_k \times 1}. \tag{11}$$

Thus, the SA data vector corresponding to the range bin is

$$\bar{\boldsymbol{s}} = \begin{bmatrix} \boldsymbol{s}1 \\ \vdots \\ \boldsymbol{s}k \\ \vdots \\ \boldsymbol{s}K \end{bmatrix}_{\bar{M} \times 1}. \tag{12}$$

We note that the SA vector has $\bar{M} = L_1 + L_2 + \cdots + L_K (\bar{M} < M)$ pulses. To clarify the expression, we define the index of pulses consisting of the valid apertures in SA data as $\bar{\boldsymbol{I}} = \left[\bar{\boldsymbol{I}}_1^T \quad \cdots \quad \bar{\boldsymbol{I}}_K^T\right]^T_{\bar{M} \times 1}$, and the index of pulses corresponding to FA data as $\boldsymbol{I} = \left[1 \quad 2 \quad \cdots \quad M\right]^T_{M \times 1}$.

III. EIGENVECTOR-BASED AUTOFOCUS AND SIGNAL RECONSTRUCTION

A. Eigenvector-Based Autofocus for SA Data of Maneuvering Targets

Together with time-variant Doppler, most existing autofocus approaches fail to remove the phase error in the SA data. However, there is one exception: the eigenvector-based autofocus method. It was first proposed in [36] and employed to correct phase error for compressed ISAR imaging in [23]. Different from conventional phase correction, the method estimates the phase error from the eigenvector corresponding to the largest eigenvalue. It has no requirement on the aperture pattern and is suitable to SA-ISAR imaging of nonmaneuvering targets. In this section, we introduce some modifications to the eigenvector-based autofocus method in terms of phase correction for maneuvering targets with SA measurements. The modified eigenvector-based autofocus method includes the following steps:

1) *Sample Selection*: For a man-made target, some range gates usually have dominant scattering centers. These range gates are optimal samples in the eigenvector-based autofocus approaches because of their high signal-to-noise ratio (SNR), which makes the estimation more efficient and precise. The amplitude of a

range cell with a dominant scatterer has small variance. The minimum variance criteria for sample selection [24] is applicable not only in conventional ISAR processing but also in SA-ISAR cases. Contrast [35] also is another useful selection criteria. Suppose N dominant range cells are selected, then the nth selected range cell may be given by

$$\bar{\boldsymbol{s}}^n = \delta^n \cdot \begin{bmatrix} e^{-j\left[2\pi\left(f_n\Delta T+\frac{1}{2}\gamma_n\Delta T^2\right)+\varphi(1)\right]} \\ \vdots \\ e^{-j\left[2\pi\left(f_nm\Delta T+\frac{1}{2}\gamma_n(m\Delta T)^2\right)+\varphi(m)\right]} \\ \vdots \\ e^{-j\left[2\pi\left(f_nM\Delta T+\frac{1}{2}\gamma_n(M\Delta T)^2\right)+\varphi(M)\right]} \end{bmatrix}_{\bar{M}\times 1} + \boldsymbol{\sigma}^n\, m \in \bar{\boldsymbol{I}}, \tag{13}$$

where δ^n represents the complex amplitude of the nth dominant range cell, $\boldsymbol{\sigma}^n$ denotes a complex white Gaussian noise, and f_n, γ_n, and $\varphi(m)$ stand for Doppler frequency, chirp rate, and the phase error in the mth pulse, respectively. The selected range cells are aligned into the following matrix $\bar{\boldsymbol{s}}$:

$$\bar{\boldsymbol{s}} = \left[\bar{\boldsymbol{s}}^1 \quad \cdots \quad \bar{\boldsymbol{s}}^n \quad \cdots \quad \bar{\boldsymbol{s}}^N\right]_{\bar{M}\times N} + \boldsymbol{\Phi}_{\bar{M}\times N}. \tag{14}$$

2) *Doppler Frequency Compensation*: For the selected range of cells, after zero-padding in the vacant apertures and Fourier transform, the Doppler cell with the strongest response is circularly shifted to zero Doppler, which removes the Doppler offset. In this step, we first fulfill the vacant apertures by padding zeros, and then follow with azimuth fast Fourier transform (FFT) to obtain a blurred RD image, where the Doppler bin with the strongest response is determined. Because the Doppler offset corresponds to a linear phase in the time domain, instead of using a circular shift to move the strongest response to the zero Doppler, we multiply the corresponding linear phase function with the zero-padded signal in the time domain. The vacant apertures are removed from the time domain data directly after multiplication. Assuming the Doppler frequency of each dominant range cell is removed, the signal is given in the form

$$\bar{\boldsymbol{s}}^n = \delta^n \cdot \begin{bmatrix} e^{-j\left[\pi\gamma_n\Delta T^2+\varphi(1)\right]} \\ \vdots \\ e^{-j\left[\pi\gamma_n(m\Delta T)^2+\varphi(m)\right]} \\ \vdots \\ e^{-j\left[\pi\gamma_n(M\Delta T)^2+\varphi(M)\right]} \end{bmatrix}_{\bar{M}\times 1} + \boldsymbol{\sigma}^n. \tag{15}$$

It should be emphasized that in the beginning iterations, because of the presence of second-order phase terms together with phase error, the precision of Doppler frequency removal is not as optimal as expected. However, with the increase in iteration number, both second-order phase and phase error are suppressed at a low level, the strong response can represent the Doppler offset of each strong scattering center, and its removal can be achieved accurately. On the other hand, accurate Doppler offset removal feeds back to more precise phase error estimation in the following steps.

3) *Second-Order Phase Compensation.* Before the phase error estimation, the second-order phase terms of selected strong scattering centers should be removed precisely. After Doppler offset removal in the last step, $\bar{\boldsymbol{s}}^n$ chirp rate γ_n is obtained by means of an exhaustive linear search over the variable γ in a predefined interval $[\gamma_{\min}, \gamma_{\max}]$. Maximum peak is used to determine an optimal estimate, which is given by the optimization

$$\langle\hat{\gamma}_n\rangle = \max_{\gamma} peak\left\{FFT\left\{\bar{\boldsymbol{s}}^n \odot \boldsymbol{g}(\gamma)\right\}\right\}, \tag{16}$$

where $\boldsymbol{g}(\gamma) = \left[e^{j\pi\gamma\Delta T^2} \quad \cdots \quad e^{j\pi\gamma(M\Delta T)^2}\right]^T_{\bar{M}\times 1}$, $peak\{\bullet\}$ denotes the maximum element of a vector, and $FFT\{\cdot\}$ is a discrete FFT operator for a vector. After compensation of the second-order phase, the signal matrix can be written as

$$\bar{\boldsymbol{s}}^n = \delta^n \cdot \boldsymbol{\theta}_{\bar{M}\times 1} + \boldsymbol{\sigma}^n, \tag{17}$$

where $\boldsymbol{\theta}_{\bar{M}\times 1} = \left[e^{-j\varphi(1)} \quad \cdots \quad e^{-j\varphi(M)}\right]^T_{\bar{M}\times 1}$ is the vector corresponding to the phase error. Therefore, the sample matrix can be rewritten as

$$\begin{aligned} \bar{\boldsymbol{s}} &= \left[\bar{\boldsymbol{s}}^1 \quad \cdots \quad \bar{\boldsymbol{s}}^n \quad \cdots \quad \bar{\boldsymbol{s}}^N\right]_{\bar{M}\times N} \\ &= \boldsymbol{\theta}_{\bar{M}\times 1} \cdot (\boldsymbol{\alpha}_{N\times 1})^T + \boldsymbol{\Phi}_{\bar{M}\times N}, \end{aligned} \tag{18}$$

where $\boldsymbol{\alpha}_{N\times 1} = \left[\delta^1 \quad \cdots \quad \delta^N\right]_{N\times 1}$ is the amplitude vector and $\boldsymbol{\Phi}_{\bar{M}\times N}$ is the noise matrix. This step is significant for phase adjustment of SA data, by which quadratic phase terms induced by target maneuvering are corrected for all selected dominant scattering centers. As a result, the interference of quadratic phase on the phase error estimate with the eigenvector-based approach effectively is eliminated, yielding primary precision improvement of the phase adjustment.

4) *Phase Error Estimate*: In general, the variance of noise in each dominant range cell is assumed to follow an identical distribution. Let $\hat{\boldsymbol{C}} = \frac{1}{N}\overline{\boldsymbol{S}\boldsymbol{S}}^H = \frac{1}{N}\sum_{n=1}^{N}\bar{\boldsymbol{s}}^n \cdot (\bar{\boldsymbol{s}}^n)^H$. Then, the maximum likelihood estimation [9] of $\boldsymbol{\theta}_{\bar{M}\times 1}$ allows the choice of $\hat{\boldsymbol{\theta}}$ satisfying $\hat{\boldsymbol{\theta}}^H\hat{\boldsymbol{\theta}} = N$ and maximizing the function

$$Q = \hat{\boldsymbol{\theta}}^H\hat{\boldsymbol{C}}\hat{\boldsymbol{\theta}} = \sum_{n=1}^{N}\lambda_n |z_n|^2, \tag{19}$$

where the vector $\boldsymbol{z} = \left[z_1 \quad \cdots z_n \cdots \quad z_N\right]^H = \boldsymbol{P}^H\boldsymbol{\theta}_{\bar{M}\times 1}$, $\boldsymbol{P}$ is the eigenmatrix of $\hat{\boldsymbol{C}}$, and λ_1 is the eigenvalue corresponding to z_1 with $\lambda_1 \geq \lambda_2 \cdots \geq \lambda_{\bar{M}}$. Apparently, choosing $\hat{\boldsymbol{\theta}} = z_1$ maximizes Q. Phase adjustment is achieved by applying the eigenvector to correct the phase error. Thus, the eigenvector method is suitable for compensating the phase error of the SA-ISAR data.

5) *Iterative Estimation and Correction*: Phase correction of the selected range cells is performed through the phase error vector computed from the eigenvector corresponding to the maximum eigenvalue. Then steps 2, 3, and 4 are repeated in sequence. In an iterative manner, because the image of dominant range cell trends to be focused, the response of an individual dominant point becomes more compact and SNR improves. The Doppler frequency and chirp rate estimation become more precise, which in turn enhances the accuracy of phase error estimation with the eigenvector-based method. In general, convergence is achievable within only several iterations. It should be noted that using the original eigenvector autofocus approach to perform coarse phase correction is helpful in accelerating autofocus processing, and the modified eigenvector may be applied as a fine correction in a further step. In some cases in which the high-frequency phase error is characteristic, coarse correction can accelerate convergence of the proposed approach effectively. Another significant aspect of the algorithm is the stopping criteria of the iterative approach. As the estimate of phase error proceeds, Doppler frequencies and chirp rates of the samples tend to be more precise, and the largest eigenvalue λ_1 increases until convergence is achieved. One may assume it is accurate enough when the difference between the largest eigenvalues of two sequential iterations is smaller than a predetermined threshold, such as 1 percent of λ_1. To enhance the robustness of the eigenvector autofocus method in strong noise circumstances, different weights can be added to the selected dominant range cells to encourage contribution from high-quality cells to the estimate [24].

Fig. 3 shows a clear flowchart of motion compensation for SA-ISAR imaging of maneuvering targets. In the flowchart, the original and the proposed eigenvector autofocus methods are performed in sequence. The former is utilized for coarse phase compensation, and the modified method implements the fine correction.

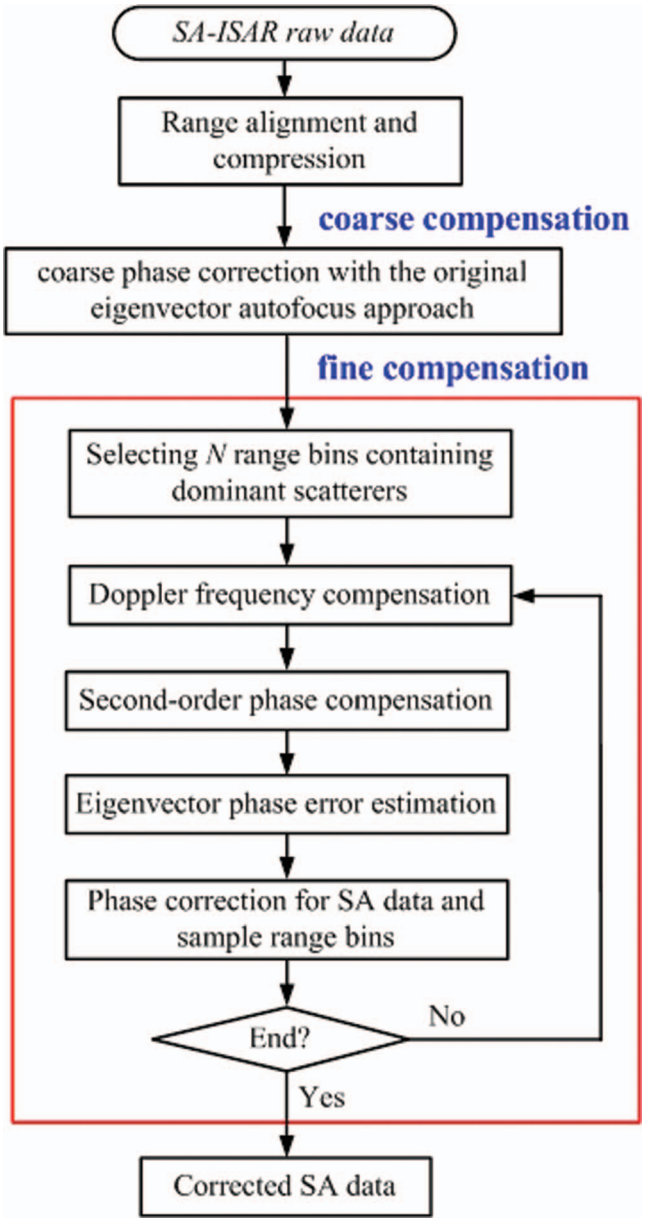

Fig. 3. Motion compensation for SA-ISAR data of maneuvering targets.

B. Full-Aperture Signal Reconstruction From SA Data

In this section, we consider FA data reconstruction from SA data. After phase error correction, the SA signal $\bar{\boldsymbol{s}}$ for a range gate is rewritten as

$$\bar{\boldsymbol{s}} = \sum_{p=1}^{P} \bar{\boldsymbol{s}}_p + \boldsymbol{\sigma}, \tag{20}$$

where P scattering centers are assumed in the range cell, and the pth component is given by

$$\bar{\boldsymbol{s}}_p(m) = \delta_p' \cdot \exp\left[-j2\pi\left(k_p\frac{m}{M} + \frac{1}{2}y_p\frac{m^2}{M^2}\right)\right] \quad m \in \bar{\boldsymbol{I}}. \tag{21}$$

Let $\gamma_p = \frac{1}{(M\cdot\Delta T)^2}\cdot y_p$ and $f_p = \frac{1}{M\cdot\Delta T}\cdot k_p$. Clearly, each signal component is a chirp with unknown Doppler frequency, chirp rate, and complex-value amplitude. For our convenient derivation, let k and y stand for the Doppler frequency and chirp rate, respectively; then, a SA chirp–Fourier basis can be constructed as

$$\bar{\boldsymbol{d}}(k, y) = \frac{1}{\sqrt{\bar{M}}}\cdot \boldsymbol{F}_k \odot \boldsymbol{C}_y \tag{22}$$

$$\boldsymbol{F}_k = \left[\, w^k \quad \cdots \quad w^{km} \quad \cdots \quad w^{kM} \,\right]^T_{\bar{M}\times 1} \tag{23}$$

$$\boldsymbol{C}_y = \left[\, q^y \quad \cdots \quad q^{ym^2} \quad \cdots \quad q^{yM^2} \,\right]^T_{\bar{M}\times 1} \quad m \in \bar{\boldsymbol{I}}, \tag{24}$$

where "$\odot$" denotes Hadamard multiplication; $w = \exp\left(-j\frac{2\pi}{M}\right)$, $q = \exp\left(-j\frac{\pi}{M^2}\Delta y\right)$, and Δy is the grid step of the chirp rate. The Doppler series corresponds to $[1 : M]^T_{M\times 1}$(identical to $\boldsymbol{I}$), and the chirp rate extends to the vector $\boldsymbol{y} = [-Y/2 + 1 : Y/2]^T_{Y\times 1}\cdot\Delta y$, where Y is supposed to be an even integer and selected so that $\boldsymbol{y}$ includes the chirp rates of all signal components in (21).

We then have the SA chirp–Fourier dictionary as

$$\bar{\boldsymbol{D}} = \Big\{ \underbrace{\bar{\boldsymbol{d}}(1,1)}_{M} \quad \cdots \quad \bar{\boldsymbol{d}}(M,1) \quad \cdots \quad \cdots \quad \underbrace{\bar{\boldsymbol{d}}(1,Y)}_{M} \quad \cdots \quad \bar{\boldsymbol{d}}(M,Y) \Big\}_{\bar{M}\times(M\cdot Y)}. \tag{25}$$

In a condensed form, the SA signal of the range cell can be rewritten as

$$\bar{\boldsymbol{s}} = \bar{\boldsymbol{D}} w + \boldsymbol{\sigma}. \tag{26}$$

Our goal is to reconstruct the unknown vector $\boldsymbol{w}$ based on the definite partial chirp–Fourier dictionary $\bar{\boldsymbol{D}}$ and the SA vector $\bar{\boldsymbol{s}}$. It should be noted that the chirp-Fourier dictionary $\bar{\boldsymbol{D}}$ is deterministic but not parametric, so we do not require the target rotational parameters a priori to construct the dictionary or to estimate them by exhaustive search before image formation. The key step is in estimating the optimal parameters y_p, k_p, and δ_p for each signal component, by which the FA signal can be easily reconstructed. The ISAR imagery shows distribution of the target scattering field, where strong scattering centers usually take up only a fraction of whole image bins but contribute the major energy. Therefore, such an ISAR signal is regarded as sparse. Moreover, as range compression is applied, the limited scatterers are distributed over a set of range bins. Each range cell contains only a few scatterers rather than all scatterers of the target. As a result, $\boldsymbol{w}$ presents strong sparsity. Such sparsity is utilized to recover the high-dimension vector $\boldsymbol{w}$ by an l_1-norm optimization

$$\langle \hat{\boldsymbol{\omega}} \rangle = \arg\min_{\sigma} \|\boldsymbol{w}\|_1, \quad s.t. \ \left\|\bar{\boldsymbol{s}} - \bar{\boldsymbol{D}} w\right\|_2 \le \varepsilon, \tag{27}$$

where $\|\bullet\|_1$ denotes the l_1-norm of a vector, and $\varepsilon = \|\boldsymbol{\sigma}\|_2$ is the noise term. The noise term can be estimated by range bins containing pure noise [37]. One can see that the optimization is composed of two different terms: the l_2-norm constraint that preserves the data fidelity of the solution and the l_1-norm optimization that imposes mostly small elements, with a few large ones, in accordance with the sparsity of the ISAR signal. The optimization problem can be solved efficiently by some approaches [38–43]. However, the high dictionary dimension leads to a great computational load and memory requirement, which hinders the application of currently existing algorithms in practice. On the basis of the standard OMP algorithm, we develop an effective solver for the optimization problem (27). Implemented by FFT and interpolation, the solver is efficient and precise. The reconstruction and imaging procedure takes the following steps.

1) We need to estimate the first chirp component of $\bar{\boldsymbol{s}}$, which is $\bar{\boldsymbol{s}}e_1$. Its Doppler frequency k_1 and chirp rate y_1 are achieved when the inner product of $\bar{\boldsymbol{s}}$ and the basis in $\bar{\boldsymbol{D}}$ reach its maximum; that is,

$$\langle k_1, y_1 \rangle = \max_{k,y} \left| \bar{\boldsymbol{d}}(k,y)^H \cdot \bar{\boldsymbol{s}} \right|. \tag{28}$$

It is not difficult to understand that estimation of k_1 and y_1 is inherently limited to the grid resolution of $\bar{\boldsymbol{D}}$, namely,

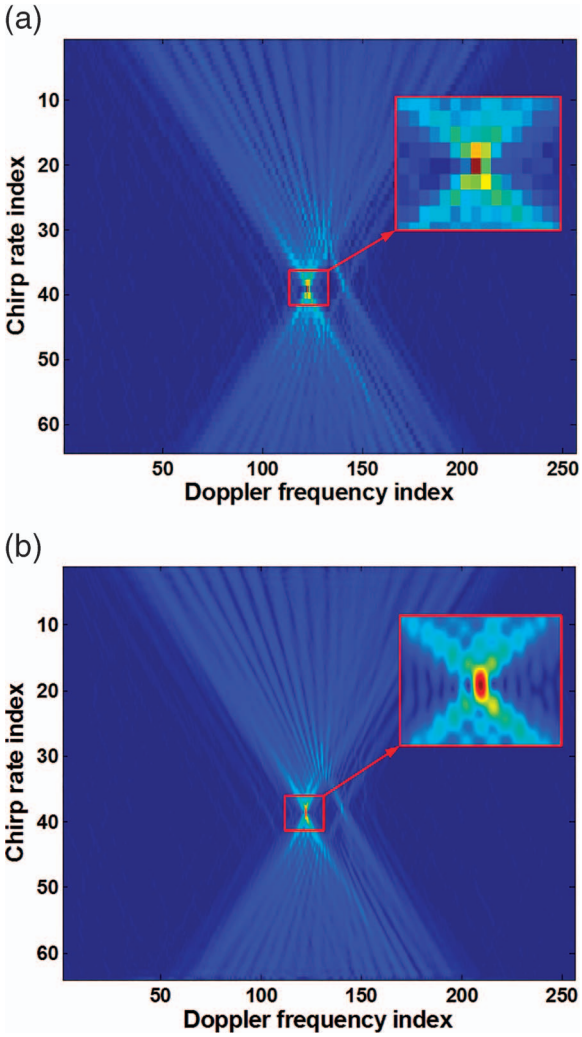

Fig. 4. Illustration of grid refinement with interpolation. (a) Before interpolation. (b) After interpolation.

the Doppler and chirp rate grids. However, if we decrease the grid steps, then the dimension of $\bar{\boldsymbol{D}}$ increases and leads to computational inefficiency. For a discrete chirp–Fourier dictionary, the chirp rate step is suggested as $\Delta y = \frac{1}{M}$ [44]. The Doppler step unit is set to avoid ambiguity. Then, we apply FFT and interpolation to enhance both precision and efficiency in the inner product computation. Suppose the inner product matrix corresponding to the dictionary is

$$\mathbf{IP}(k,y) = \bar{\boldsymbol{d}}(k,y)^H \cdot \bar{\boldsymbol{s}}. \tag{29}$$

Apparently, $\mathbf{IP}$ is an $M \times Y$ matrix. Instead of calculating its elements one by one, we may obtain a row through the computation

$$\mathbf{IP}(:,y) = FFT\left\{\bar{\boldsymbol{s}} \odot \boldsymbol{C}_y\right\}. \tag{30}$$

Before we seek the maximum element in $\mathbf{IP}$, interpolation is applied to refine its grid. Fig. 4 shows the interpolation grid refinement for $\mathbf{IP}$.

By the refined estimation of (k_1, y_1), we may achieve the signal estimate as

$$\bar{\boldsymbol{s}}e_1 = w_1 \cdot \bar{\boldsymbol{d}}(k_1,y_1) \quad \text{and} \quad w_1 = \bar{\boldsymbol{d}}(k_1,y_1)^H \cdot \bar{\boldsymbol{s}}. \tag{31}$$

2) The residual signal is calculated by $\bar{\boldsymbol{s}}_{res} = \bar{\boldsymbol{s}} - \bar{\boldsymbol{s}}e_1$.

3) We use $\bar{\boldsymbol{s}}_{res}$ to find the next basis $\boldsymbol{a}(k_2, y_2)$ with the maximum inner product criteria as shown in step 1. Then, a dictionary with two subspaces is obtained as $\bar{\boldsymbol{D}}_2 = \left[\bar{\boldsymbol{d}}(k_1, y_1), \bar{\boldsymbol{d}}(k_2, y_2)\right]$, and the corresponding amplitude is estimated by $\boldsymbol{w}_2 = \begin{bmatrix} w_1 \\ w_2 \end{bmatrix} = \left(\bar{\boldsymbol{D}}_2^H \bar{\boldsymbol{D}}_2\right)^{-1} \bar{\boldsymbol{D}}_2^H \bar{\boldsymbol{s}}$, where w_1 is renewed under $\bar{\boldsymbol{D}}_2$. The second signal estimate is obtained by $\bar{\boldsymbol{s}}e_2 = \bar{\boldsymbol{D}}_2 \cdot \boldsymbol{w}_2$.

4) Steps 2 and 3 repeat until the energy of the residual signal is below the noise level. Assume the procedure is implemented by P' iterations. The estimated parameters include: a dictionary $\bar{\boldsymbol{D}}_{P'}$ corresponding to the P' signal components, the amplitude vector $w_{P'}$, and Doppler and chirp rate vectors $\boldsymbol{k}_{P'}$ and $\boldsymbol{y}_{P'}$, which are given as

$$\bar{\boldsymbol{D}}_{P'} = \left[\bar{\boldsymbol{d}}(k_1, y_1) \quad \bar{\boldsymbol{d}}(k_2, y_2) \quad \cdots \quad \bar{\boldsymbol{d}}(k_{P'}, y_{P'})\right]_{\bar{M} \times P'}, \tag{32a}$$

$$\boldsymbol{w}_{P'} = \left[w_1 \quad w_2 \quad \cdots \quad w_{P'}\right]^T_{P' \times 1}, \tag{32b}$$

$$\boldsymbol{k}_{P'} = \left[k_1 \quad k_2 \quad \cdots \quad k_{P'}\right]^T_{P \times 1}, \tag{32c}$$

$$\boldsymbol{y}_{P'} = \left[y_1 \quad y_2 \quad \cdots \quad y_{P'}\right]^T_{P' \times 1}. \tag{32d}$$

5) After signal decomposition into the partial chirp–Fourier dictionary, with the above estimated parameters, the FA signal can be reconstructed through the formulations

$$\boldsymbol{s} = \sum_{p=1}^{P'} \boldsymbol{s}_p \quad \text{and} \quad \boldsymbol{s}_p(m) = w_p \cdot \exp\left[-j2\pi\left(k_p \frac{m}{M} + \frac{1}{2} y_p \frac{m^2}{M^2}\right)\right] \quad 1 \le m \le M. \tag{33}$$

By sparse decomposition under the chirp-Fourier dictionary, the amplitude, Doppler frequency, and chirp rate of each scattering center are achieved simultaneously. Of course, the deterministic relationship between the Doppler parameters and target rotation variables in (6) is not clear so far; however, the achievement of RID images is straightforward. The time frequency (TF) slice of the range bin may be computed through the Wigner–Ville distribution (WVD) [45] to each reconstructed signal component

$$TF = \sum_{p=1}^{P'} \boldsymbol{WVD}\left\{\boldsymbol{s}_p\right\}. \tag{34}$$

After the FA reconstruction for all range bins, their TF slices are arrayed to generate a sequence of RID images as traditional AJTFA-based ISAR images for maneuvering targets. Of course, RID images generated with (34) are of high resolution and free of cross-terms, but the computational load in (34) is relatively high. Efficient TF representations, such as adaptive optimal kernel TF representation [46], can be used on the reconstructed signal $\boldsymbol{s}$ to leverage a balance between resolution and cross-terms in RID images.

C. Extensions to MTRC Cases

The above introduction of both the autofocus approach and FA reconstruction does not account for MTRC caused by rotation. In high-resolution ISAR imaging of targets with large size, MTRC is usually present. With accommodation of some useful techniques, the negative effects of MTRC on the eigenvector autofocus and FA data recovery can be overcome effectively.

To reduce the degradation of the eigenvector autofocus approach in the presence of MTRC, we can perform the phase error estimation on the raw data at a lower resolution by down-sampling. Down-sampling is first used in [47] to reduce the influence of residual range cell migration on the phase autofocus for SAR data. Herein, this process eliminates MTRC by summing several neighboring range bins into a single bin. Also, the processing can be implemented by extracting only a part of the frequency band from the raw data to obtain the range-compressed data block [47], which is similar to summing up processing. Combining adjacent range bins should cover the range of MTRC. Then, range bin samples are selected from the down-sampled SA data for phase error estimation, but phase compensation is performed on the original SA data.

For maneuvering targets, the magnitude of MTRC depends on the target size and rotation angle within CPI. In general, rotation-induced MTRC is restricted within only several range gates in real scenarios, because a small rotation angle can be used to achieve high resolution in azimuth (e.g., ~3–5 deg). Subband division processing may be leveraged to reduce degradation of the SA data reconstruction when MTRC arises. In the FA data reconstruction after phase correction, the SA data are split into several subbands in the range frequency domain, and each subband signal is transformed back into the range-compressed domain. Similar to down-sampling processing, MTRC is eliminated because of the decrease of range resolution. Then, the FA data reconstruction of each subband is performed independently. The FA data of an entire frequency band are constructed by combining the recovered FA subband data sets together. It should be emphasized that during the subband procedure, the frequency band division is also deficient. As the resolution decreases in each subband signal, signal sparsity is reduced as well, since the number of scattering centers within a single range gate may increase. The SNR is distinctively reduced, as well. The decrease in sparsity and SNR may degrade the performance of FA signal reconstruction. In this sense, the number of subbands should be preferred to suppress MTRC and simultaneously retain the precision of FA reconstruction. Empirically, the rotation-induced MTRC is usually slight, and the frequency band of SA data can be separated into several subbands. For example, we can separate the data into four subbands, which indicates that the MTRC varying within four range cells can be overcome by the subband division. After reconstruction, MTRC should be

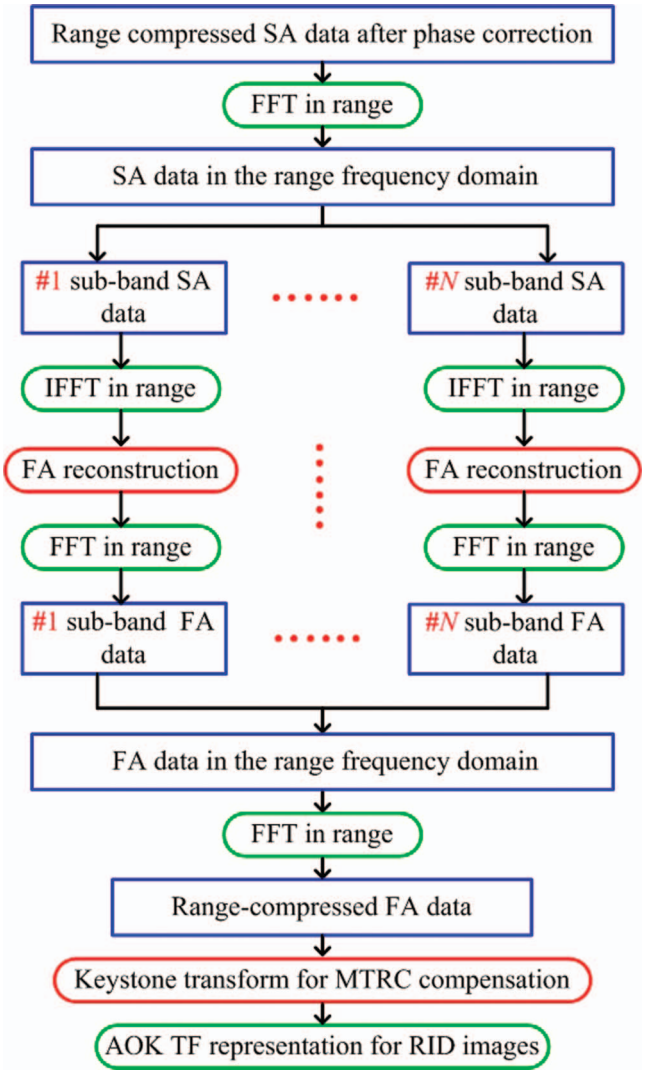

Fig. 5. Flowchart of FA reconstruction and RID imaging with subband division.

compensated on the FA data. Keystone transform [48, 49] removes the linear MTRC on the reconstructed FA data effectively by eliminating the first-order coupling term in the frequency domain. After the correction of MTRC, AJTFA algorithms are ready to generate RID images. In summary, FA reconstruction with the subband technique for MTRC cases is illustrated by the flowchart in Fig. 5.

From the flowchart, one can find evident differences in the proposed ISAR imaging procedure from ISAR formations with conventional sparse representations. Instead of direct ISAR image formation from incomplete measurements with the sparsity constraint optimization, in the proposed scheme, FA data reconstruction from SA measurements is first performed via sparse representation under a redundant chirp–Fourier dictionary, and then conventional MTRC correction follows. Finally, the ISAR image of the maneuvering target is generated by using AJTFA approaches through the reconstructed data. The MTRC correction on the FA data plays a significant role in resolving the coupling between range and azimuth dimensions. Moreover, because both FA reconstruction and AJTFA imaging are performed in azimuth, the whole SA-ISAR imaging scheme involves only one-dimensional sparse decomposition, not two-dimensional (2D) decomposition as in other sparse decomposition–based imaging algorithms [50, 51], yielding efficiency enhancement at a possible price of precision loss. Another significant reason why conventional AJTFA imaging is required in our scheme is because, as Fig. 1 shows, the effective rotational vector of maneuvering targets is time-varying during the CPI. Conventional RD imaging approaches are based on a 2D rotation model; that is, the effective rotational vector is fixed during the CPI, which is not suitable for maneuvering cases. However, AJTFA imaging can generate a sequence of RID images to adjust the change in direction of image planes during the CPI, and the RID images also pave a possible way to analyzing the aspect change of target during CPI.

IV. EXPERIMENTS

A. Simulated Data Description

This subsection comprises two parts. First, we analyze the performance of the proposed eigenvector autofocus approach for the SA-ISAR data of maneuvering targets and compare with the original eigenvector method. Second, the FA data reconstruction is tested, and its performance metrics are evaluated.

The data set applied in this subsection is the B727 plane data simulated by the Naval Research Lab. Some radar system parameters are listed as follows: The center frequency is 9 GHz, the pulse repeat frequency is 20 kHz, the FA data set consists of 256 pulses in total, and the signal bandwidth is 150 MHz. The range profiles are presented in Fig. 6(a). Considerable maneuvering causes serious blurring of the RD image, as shown in Fig. 6(b). From Fig. 6(a), one can note that explicit MTRC arises in the range-compressed data. In the following experiments, the frequency band of SA data is divided into four subbands in the FA data reconstruction with sparse representation to reduce the negative effects from MTRC. The original data set is free of phase noise. SA-ISAR data with different SNRs (from 0 to 20 dB) are generated by extracting pulses from the original data set and adding complex white Gaussian noise. Herein, SNR is defined as the ratio of signal energy and noise energy.

In some special situations, multisource phase error has substantial high-frequency properties. For example, severe vibration of both the target or radar platform together with jetting of analog/digital sampling and signal transmission could cause random phase errors. Of all type of phase errors, random errors are the most complicated and severe, and usually the most difficult to correct. To show the robustness of the eigenvector-based autofocus approaches, random phase is added (see Fig. 7) in all experiments.

To evaluate the performance of phase error estimation, the standard deviation between the estimated and the

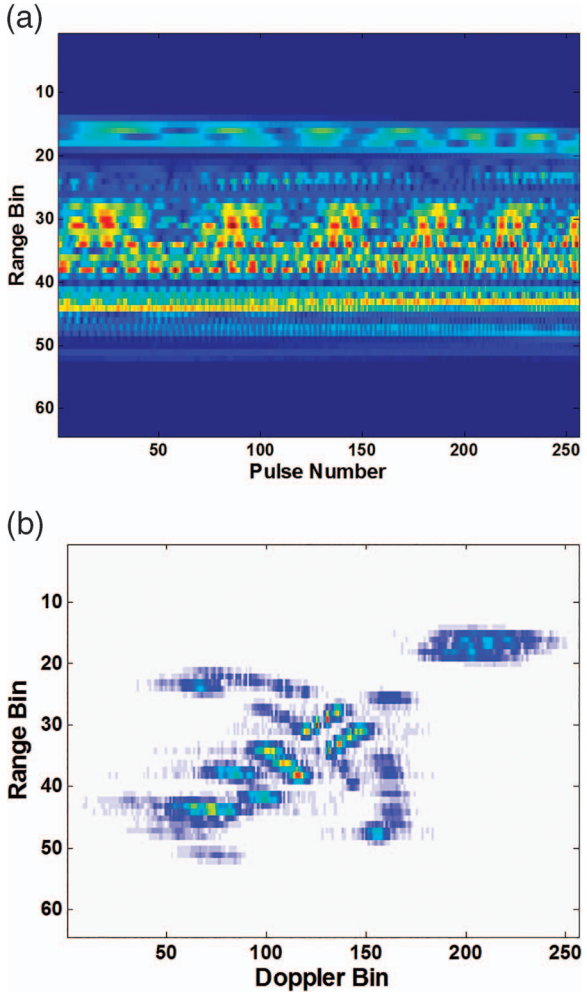

Fig. 6. Simulated B727 data. (a) Aligned range profiles. (b) RD image with serious blur.

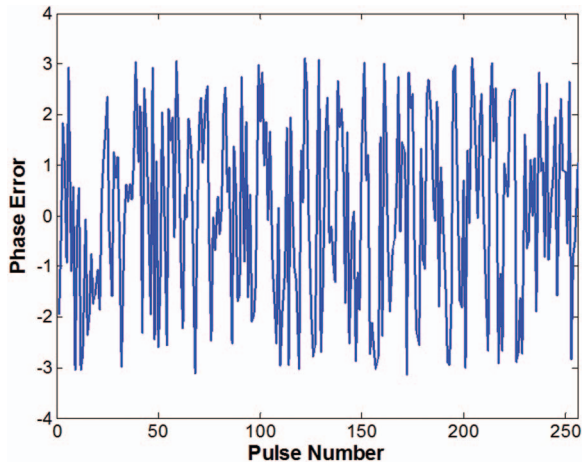

Fig. 7. Added random phase error (unit is radian).

actual added phase error is used, as in

$$\mathrm{STD} = \mathrm{std}\left[\hat{\boldsymbol{\theta}} - \boldsymbol{\theta}\right], \tag{35}$$

where std [•] denotes the operator calculating the standard deviation of a vector. The performance of FA

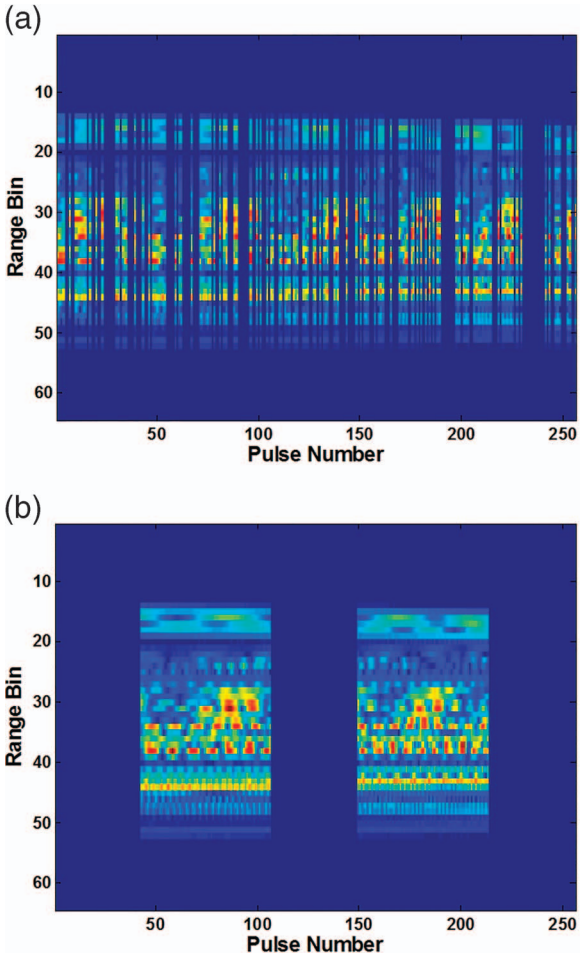

Fig. 8. Sparse aperture patterns. (a) SA-1. (b) SA-2.

reconstruction is evaluated by two factors: noise interference and pulse number. To provide a quantitative evaluation for the performance of the FA reconstruction, we view the coherence coefficient of the reconstruction and the original data as a metric, which is defined as

$$R_{coef} = \frac{\left\langle \mathbf{S} \odot \hat{\mathbf{S}} \right\rangle}{|\mathbf{S}|_F \cdot \left|\hat{\mathbf{S}}\right|_F}, \tag{36}$$

where $\mathbf{S}$ and $\hat{\mathbf{S}}$ denote the original FA and reconstructed FA data sets, respectively, and the symbol $\langle\cdot\rangle$ is the operator for summing up all components of a matrix. Apparently, when R_{coef} is close to 1, the FA data reconstruction is optimal and close to the ideal signal, whereas low R_{coef} indicates serious reconstruction degradation.

B. Performance Versus SNR

The aim of the first experiment is to analyze the influence of SNR on the performance of the various approaches. To compare noise tolerance of the original eigenvector and the proposed autofocus approaches, we consider three different aperture patterns: full aperture, random sampled SA (SA-1), and block sampled SA (SA-2). SA-1 and SA-2 are shown in Figs. 8(a) and 8(b),

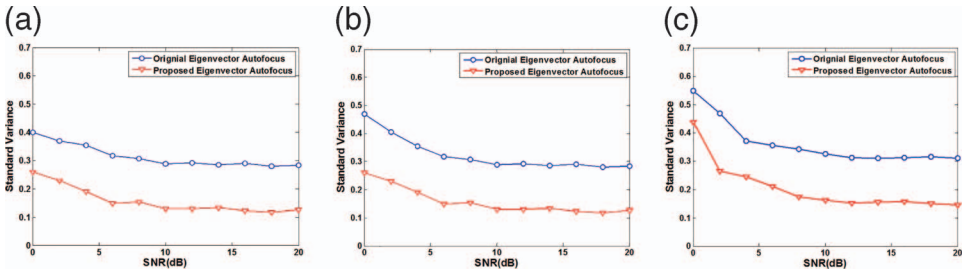

Fig. 9. Standard deviations of phase estimate errors. (a) Full-aperture case. (b) SA-1 case. (c) SA-2 case.

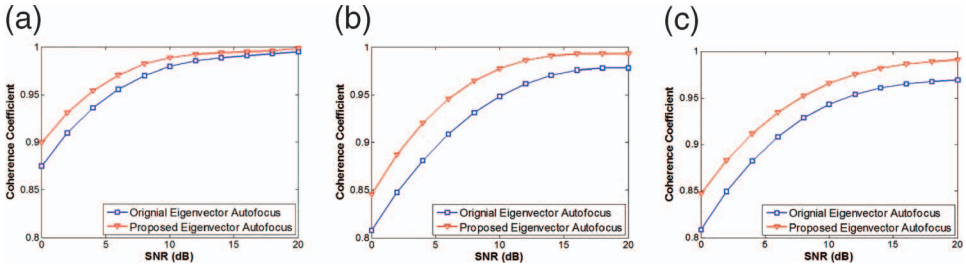

Fig. 10. Coherence coefficients with respect to SNRs. (a) Full-aperture case. (b) SA-1 case. (c) SA-2 case.

respectively. Both consist of 128 pulses. We generate experimental data sets with different SNRs (from 0 to 20 dB). The two autofocus approaches are conducted to estimate phase errors, and the standard deviations are calculated corresponding to the ideal phase error in Fig. 7. Before the computation of standard deviations, the linear and quadratic phase terms within the estimates are removed. During the proposed eigenvector autofocus approach, at least three iterations are usually needed to guarantee convergence. With respect to SNR and standard deviation curves corresponding to the three aperture patterns, three comparisons are shown in Figs. 9(a), 9(b), and 9(c), respectively. The standard deviation curves evaluate the estimated accuracy of the two eigenvector-based autofocus approaches. From Fig. 9, one can see that the performance of the two algorithms depends on SNR, and strong noise degrades their performance distinctively. In all cases, the proposed eigenvector method achieves lower standard deviations than does the original eigenvector method. This indicates that high accuracy is achieved by the modified eigenvector approach. Because the proposed eigenvector accounts for the time-varying Doppler characteristic of the target signal, a better phase estimate is achieved, as presented in Fig. 9, which consequently supports optimal FA reconstruction from SA measurements and RID imaging of maneuvering targets.

After phase correction, the recovery of FA data follows in sequence. The same processing is performed for the full-aperture pattern data, which can be regarded as signal decomposition and denoising. Thus, the reconstructions for the three aperture patterns are compared with the original FA data in Fig. 10(a) by calculating their coherence coefficients with the reference data set. In the analysis, we perform Monte Carlo analyses with 100 signal cases. The mean values of coherence coefficients have been exploited to evaluate FA reconstruction performance. In the three cases, the smoothed coherence coefficient curves with respect to SNR are shown in Figs. 10(a), 10(b), and 10(c), respectively. Fig. 10 shows that the FA reconstruction depends on SNR and autofocus approaches distinctively, and the coherence coefficient curves are also in accordance with the phase estimate standard deviation curves in Fig. 8. When noise increases, the reconstruction deviates from the ideal signal correspondingly, no matter which autofocus approach is applied. Because the proposed eigenvector autofocus approach overcomes the phase error in a more precise manner, it obtains better reconstruction performance than does the original eigenvector autofocus method. This result is evident by both precision of the phase correction and reconstruction in all cases. One can see that, in both SA cases, the coherence coefficients are high—up to 0.95—with SNR up to 10 dB if the proposed autofocus approach is utilized. However, the original autofocus approach cannot ensure this reconstruction performance even in high-SNR scenarios.

To show the effectiveness of the phase adjustment and FA reconstruction for the three data sets, RID images are generated according to the procedure in Fig. 11. Three instantaneous moments (t1, t2, and t3) correspond to the 64th, 128th, and 192nd pulse, respectively. In this section, all RID images are shown in decibels with identical scales.

First, we look at the full-aperture case. Figs. 11(a) and 11(b) show the resulting RID images with different SNRs (4 and 8 dB) in the full-aperture case. Fig. 11(a) shows the RID images using the original autofocus approach, and Fig. 11(b) shows RID images from the proposed autofocus

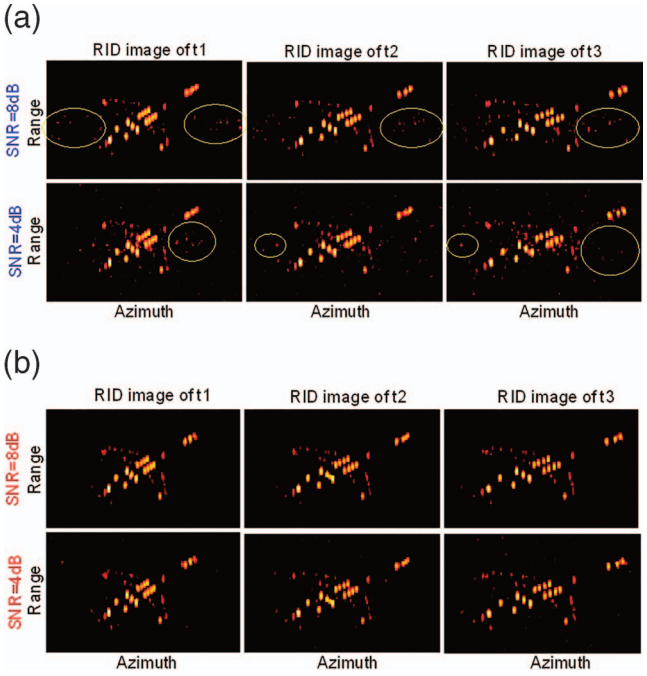

Fig. 11. RID images with full-aperture data under different SNRs. (a) Images from original autofocus approach. (b) Images from the proposed autofocus approach.

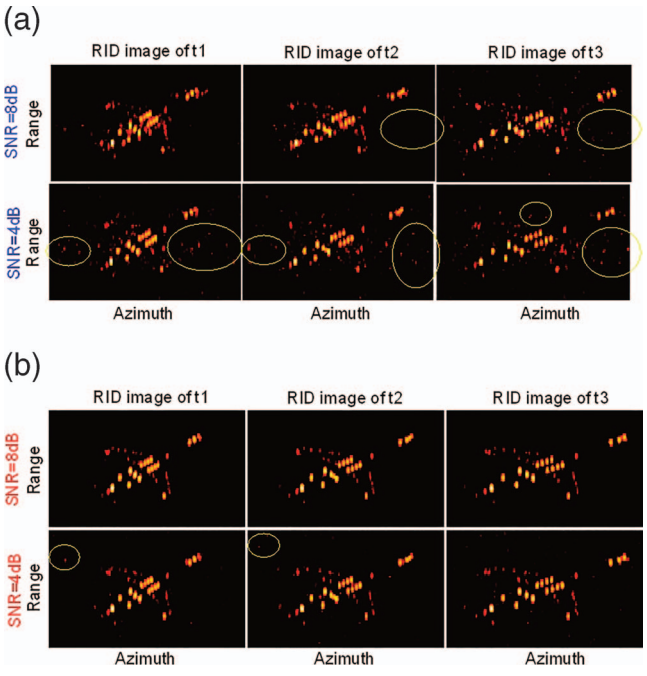

Fig. 12. RID images with SA-1 signal under different SNRs. (a) Images from original autofocus approach. (b) Images from the proposed autofocus approach.

method. Generated by the FA reconstruction signal after the proposed autofocus processing, RID images are free of blurring and noise. However, after phase correction with the original autofocus method, significant residual phase error exists, which consequently causes degradation of the following FA reconstruction and RID imaging. As a result, some blur and false points are present in Fig. 11(a). For a clear comparison, we highlight the image regions contaminated by false points with circles. The image degradation with increased noise is also evident in the RID images, since false points are present when SNR decreases down to 4 dB, and this phenomenon is not evident when we apply the proposed autofocus approach, as seen in the resulting RID images in the 4-dB case compared with those in the 8-dB case. This result may be a case in which optimal phase error removal would improve the denoising performance in the RID images.

In the following discussion, we investigate the SA imaging case. Fig. 12 shows typical RID images with different SNRs (4 and 8 dB) in the SA-1 case, and Fig. 13 images show the SA-2 case. Figs. 12(a) and 13(a) show the RID images with phase adjustment by the original autofocus approach; meanwhile, Figs. 12(b) and 13(b) have RID images with phase correction by the proposed autofocus method. In both Figs. 12 and 13, the first row presents RID images corresponding to the three instantaneous times under SNR = 8 dB. The second row gives RID images under SNR = 4 dB. Given a close insight into the details of the RID images, we can find that all images are focused, but those from the proposed approach are more precise. The first conclusion that should be emphasized is the effectiveness of

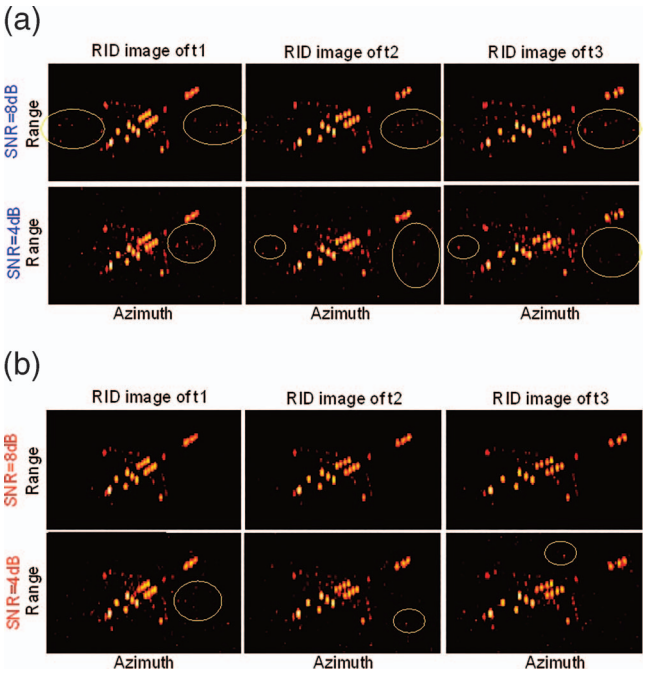

Fig. 13. RID images with SA-2 signal under different SNRs. (a) Images from original autofocus approach. (b) Images from the proposed autofocus approach.

eigenvector-based autofocus processing for SA data sets. Accommodating the time-varying Doppler characteristic of the signal, the proposed autofocus method achieves higher precision, yielding optimal FA reconstruction and RID imaging performance in both SA cases. We also highlight the regions containing false points with circles in both Fig. 12 and Fig. 13. Image degradation with increase

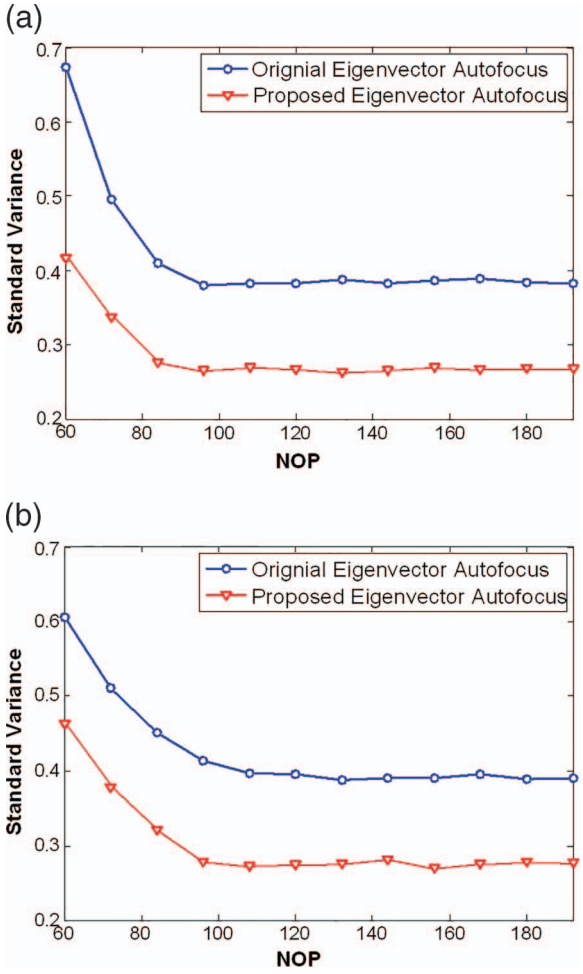

Fig. 14. Standard deviations with respect to NOPs. (a) SA-1 case. (b) SA-2 case.

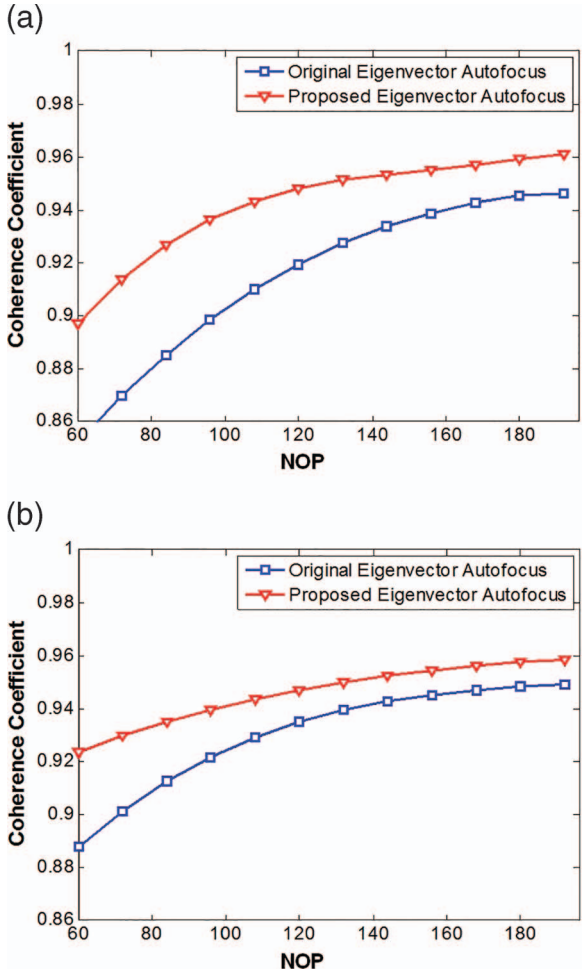

Fig. 15. Coherence coefficients with respective to NOPs. (a) SA-1 case. (b) SA-2 case.

in noise is also evident in the RID images, especially with the original autofocus method when SNR decreases down to 4 dB. Nevertheless, the high quality of RID images generated by the proposed autofocus method remains when noise increases, which is very close to that in the FA data case.

C. Performance Versus Pulse Number

We now investigate how the sample amount affects recovery performance. We test the reconstructed results of the two SA patterns by varying the number of pulses (NOP). With different numbers of pulses and constant SNR (8 dB), we first correct the SA data sets by the proposed eigenvector autofocus method and then reconstruct the FA signal and RID images. The pulse number is set to decrease from 196 to 60. The standard deviation curves reveal the estimate accuracy of the two eigenvector-based autofocus approaches, as shown in Fig. 14, and the coherent coefficient curves are shown in Fig. 15. One can see that, with relatively high SNR, a highly coherent coefficient is achievable, which indicates optimal recovery in both SA cases, and the reconstructed FA signal is closer to the ideal data. This phenomenon is not explicit when the pulse amount is small, such as NOP = 60, because the coherence coefficient decreases down to a small value.

Figs. 16 and 17 show typical RID images with two different SA pulse amounts (108 and 60), by which we investigate the performance of approaches with specific pulse numbers. By comparing Figs. 16 and 17, in all cases, the proposed approaches are capable of precisely reconstructing the FA signal and generating RID images with high quality in both SA patterns. Inspecting Figs. 16 and 17, we find that although the original eigenvector autofocus approach works in both SA cases, its performance may be still unacceptable simply because the error and false points (highlighted by circles) degrade the RID image to some degree. We can make this inference because the focal quality of the RID image of the maneuvering target obtained using the proposed phase adjustment and FA reconstruction is satisfactory. These results indicate that the proposed phase correction suppresses phase error optimally by considering the time-varying Doppler of the target signal and is suitable for generating high-quality RID images by combining the FA reconstruction based on sparse representation.

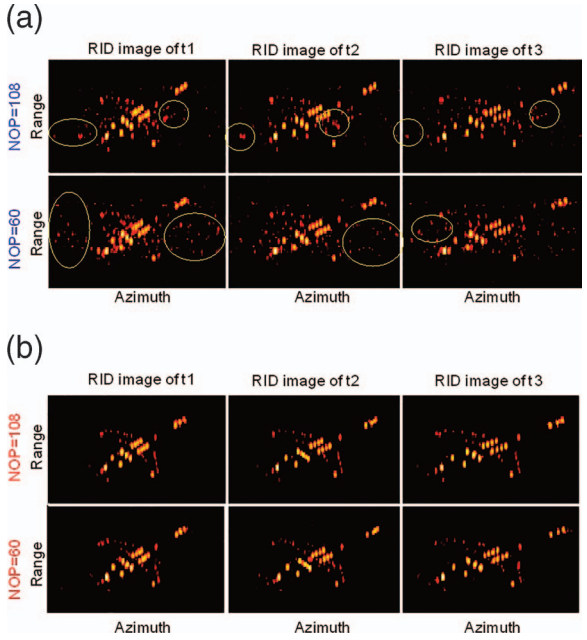

Fig. 16. SA-1 RID images under different pulse numbers (in decibels). (a) Original eigenvector autofocus. (b) Proposed eigenvector autofocus.

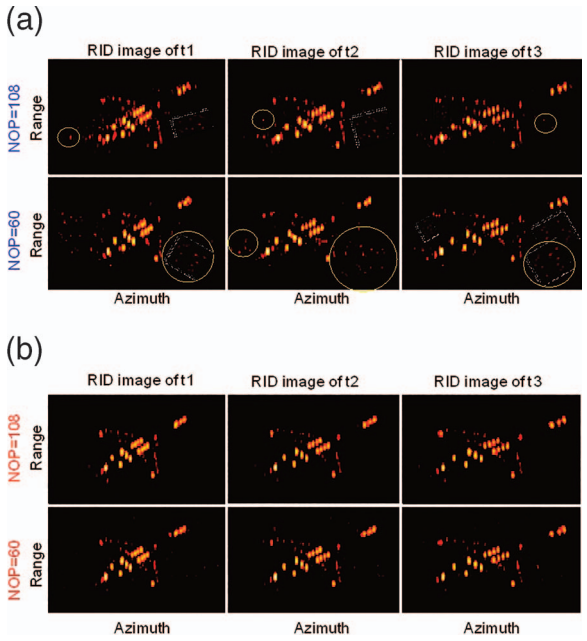

Fig. 17. SA-2 RID images under different pulse numbers (in decibels). (a) Original eigenvector autofocus. (b) Proposed eigenvector autofocus.

D. Real Data Experiments

In this subsection, real, measured data are utilized to test the performance of the proposed methods. The data set of a Yak-42 airplane is recorded by a C-band (5.52 GHz) ISAR experimental system. The transmitting signal is a 400-MHz linear modulated chirp signal. The received signal is dechirped and I/Q sampled. In this data set, the pulse repetition frequency is 100 Hz (i.e., 256 pulses are used). Range alignment is performed to remove the range shift induced by translational motion in advance.

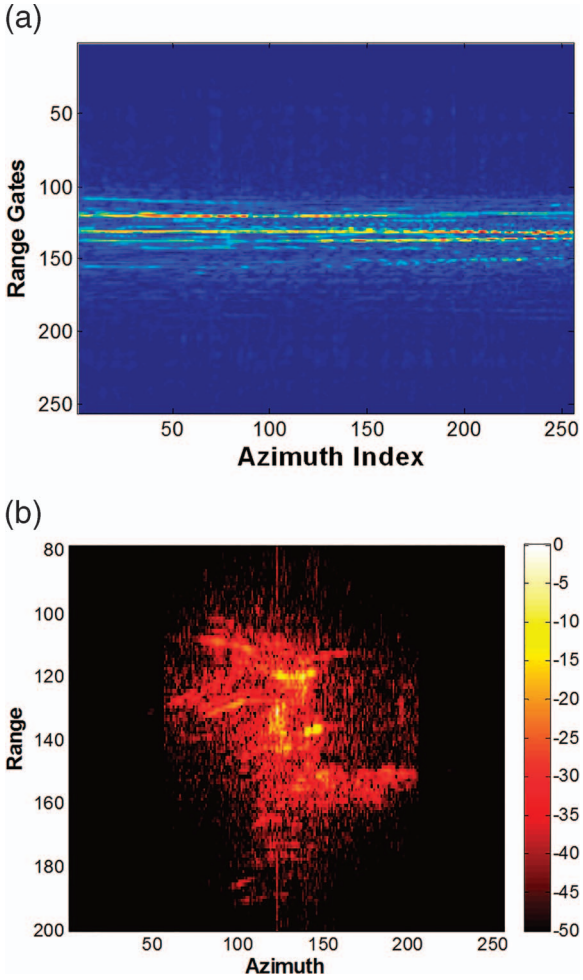

Fig. 18. Yak-42 data and RD image. (a) Aligned range profiles. (b) RD image.

Significant movement is involved during target maneuvering. As a result, not only time-varying Doppler but also explicit MTRC are induced in the recorded data. The aligned profiles are shown in Fig. 18(a), where MTRC can be inspected clearly. The RD image generated by all 256 pulses after phase correction with the eigenvector autofocus is shown in Fig. 18(b). Maneuvering during observation causes evident RD image smearing. The original recorded data has considerable noise, so we do not add any synthesized noise into the data. SA data sets with 128 pulses are generated by extracting pulses from the original data. A random sampled SA pattern is assumed. In FA reconstruction processing, data sets are divided into four subbands in the frequency domain to reduce the negative effect from MTRC. Keystone transform is applied to the reconstructed FA data for MTRC removal before RID image processing. At first, we investigate the autofocus performance of both the original and proposed eigenvector approaches with the full aperture data. The AJTFA RID images corresponding to the three instantaneous moments are provided in Figs. 19(a) and 19(b). Their image contrast and entropy are also calculated to investigate focal performance. The effectiveness of

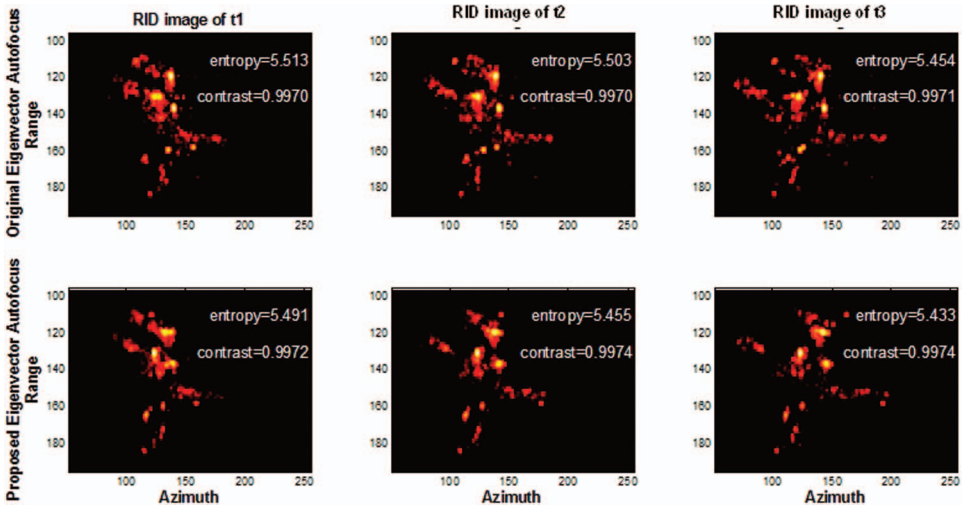

Fig. 19. FA experiment results.

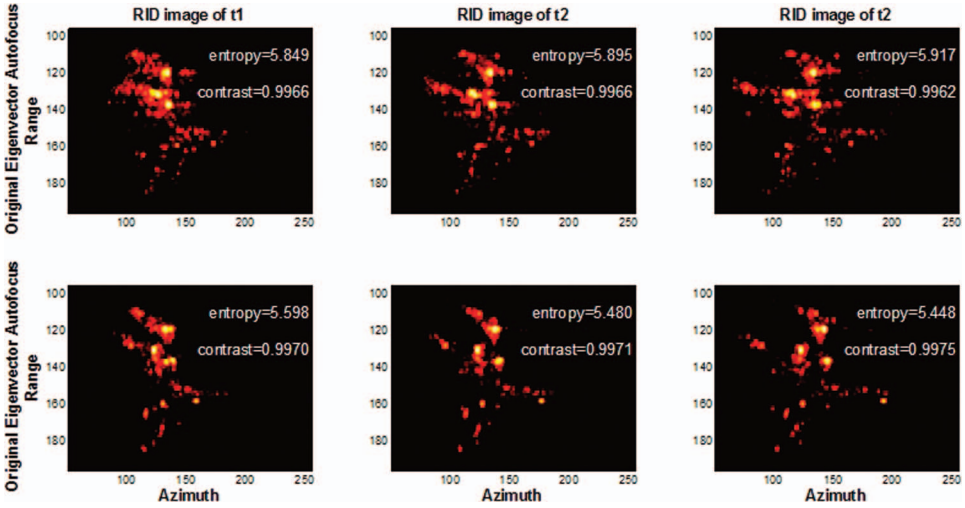

Fig. 20. SA experiment results.

eigenvector autofocus methods for the maneuvering airplane is confirmed. From Fig. 19, one can see that, for the maneuvering characteristic of the target, the proposed autofocus approach removes the phase error optimally, yielding significant focal improvement over the original approach. As can be seen, some evident blurs in Fig. 19(a) are eliminated in Fig. 19(b). Next, we investigate the SA case. The RID images are arrayed in Figs. 20(a) and 20(b) for comparison. As expected, ideal FA reconstruction is not available because we cannot remove the phase error correctly with the original autofocus approach, which is inferred, in that the coherence coefficient of FA reconstruction and ideal data is only 0.911. However, when the proposed autofocus approach is applied, we can get better FA reconstruction, and the coherence coefficient is up to 0.942. With a high-coherence coefficient of FA reconstruction, the AJTFA RID imaging scheme apparently provides ideal focusing performance (Fig. 20(b)), exhibiting the geometrical structure of the target. In terms of image entropy and contrast, the performance improvement of the proposed algorithms is shown clearly. One should also note that residual phase error affects the FA reconstruction dramatically, consequently leading to considerable focal loss and false points in the RID images, as shown in Fig. 20(a).

V. CONCLUSIONS

ISAR imaging by SA data is essential for multifunctional radar because it is capable of furnishing a single radar system with the imaging ability of multiple uncooperative targets. In this paper, we focused on phase correction and signal reconstruction in SA-ISAR imaging of maneuvering targets. A modified eigenvector-based autofocus approach was proposed that can correct the high-frequency phase error within SA data of a maneuvering target. Improvement by a modified eigenvector–based autofocus approach over the traditional one is demonstrated. Instead of direct ISAR formation from incomplete measurements with conventional sparse optimization approaches, in the proposed image scheme, FA data reconstruction from SA measurements is first

performed via sparse representation under a redundant chirp–Fourier dictionary. Then, conventional MTRC correction can be applied to the FA data. Finally, an ISAR image of the maneuvering target is generated by AJTFA approaches through the reconstructed data. This procedure is flexible and efficient for imaging maneuvering targets in real scenarios. Both simulated and real data experiments validate the effectiveness of the proposed approaches for the SA-ISAR imaging of maneuvering targets. Finally, it should be pointed out that sparse decomposition paves a potential way to bridge the Doppler parameters to target rotation during RID image formation. And if a deterministic relationship between them can be developed, rotation estimation and azimuth scaling for a maneuvering target image is possible. Some important problems, such as shadow and amplitude modulation in signal modeling, are ignored, which limits application of the proposed method in some real scenarios. These problems will be investigated in the near future.

ACKNOWLEDGMENT

The authors thank the anonymous reviewers for their valuable comments to improve the quality of this paper.

REFERENCES

[1] Herd, J., Duffy, S., Webar, M., Brigham, G., Weigand, C., and Cursio, D.
Low cost multifunction phased array radar concept.
In *Proceedings of the 2010 IEEE International Symposium on Phased Array Systems and Technology (ARRAY)*, Lexington, MA, Oct. 12–15, 2010, 457–460.

[2] Pastina, D., Bucciarelli, M., and Lombardo, P.
Multistatic and MIMO Distributed ISAR for Enhanced Cross-Range Resolution of Rotating Targets.
IEEE Transactions on Geoscience and Remote Sensing, **48**, 8 (Aug. 2010), 3300–3317.

[3] Larsson, E. G., Liu, G. Q., Stoica, P., and Li, J.
High-resolution SAR imaging with angular diversity.
IEEE Transactions on Aerospace and Electronic Systems, **37**, 4 (Oct. 2001), 1359–1372.

[4] Larsson, E. G., Stoica, P., and Li, J.
Amplitude spectrum estimation for two-dimensional gapped data.
IEEE Transactions on Signal Processing, **50**, 6 (June 2002), 1343–1353.

[5] Larsson, E. G., and Li, J.
Spectral analysis of periodically gapped data.
IEEE Transactions on Aerospace and Electronic Systems, **39**, 3 (July 2003), 1089–1097.

[6] Li, H. J., Farhat, N. H., and Shen, Y. S.
A new iterative algorithm for extrapolation of data available in multiple restricted regions with applications to radar imaging.
IEEE Transactions on Antennas. Propagation, **AP-35**, 5 (May 1987), 581–588.

[7] Cabrera, S. D. and Parks, T. W.
Extrapolation and spectral estimation with iterative weighted norm modification.
IEEE Transactions on Signal Processing, **39**, 4 (Apr. 1991), 842–851.

[8] Xu, X., Huang, P. and Feng, X.
An iterative algorithm for ultra wideband radar imaging from randomly fragmented spectral data.
In *Proceedings of the SEE 2004 Radar Conference*, Toulouse, France, Oct. 2004.

[9] Tsao, J., and Steinberg, B. D.
Reduction of sidelobe and speckle artifacts in microwave imaging: the CLEAN technique.
Transactions on Antennas and Propagation, **36**, 4 (Apr. 1988), 543–566.

[10] Bose, R.A., Freeman, A., and Steinberg, B. D.
Sequence CLEAN: a modified deconvolution technique for microwave images of contiguous targets.
IEEE Transactions on Aerospace and Electronic Systems, **38**, 1 (Jan. 2002), 89–96.

[11] Cetin, M. and Moses, R. L.
SAR imaging from partial-aperture data with frequency-band omissions.
In *Proceedings of SPIE Defense and Security Symposium, Algorithm for Synthetic Aperture Radar Imaging* XII, Orlando, FL, Mar. 2005.

[12] Zhang, B. C., Hong, W., and Wu, Y. R.
Sparse microwave imaging: Principles and applications.
Science China Information Sciences, **55**, 8 (2012), 1722–1754.

[13] Onhon, N. O., and Cetin, M.
A nonquadratic regularization-based technique for joint SAR imaging and model error correction.
In *Proceedings of SPIE, Algor. Synthetic Aperture Radar Imagery XVI*, vol. 7337, article 73370C, 2009, 10 p.

[14] Bao, Z., Wang, G., and Luo, L.
Inverse synthetic aperture radar imaging of maneuvering targets.
Optical Engineering, **37**, 5 (May 1998), 1582–1588.

[15] Wu, L., Wei, X. Z., Yang, D. G., Wang, H.Q., and Li, X.
ISAR Imaging of Targets With Complex Motion Based on Discrete Chirp Fourier Transform for Cubic Chirps.
IEEE Transactions on Geoscience and Remote Sensing, **50**, 10 (Oct. 2012), 4202–4212.

[16] Wang, Y., and Jiang, Y.
ISAR imaging of a ship target using product high order matched-phase transform.
IEEE Geoscience and Remote Sensing Letters, **6**, 4 (Oct. 2009), 658–661.

[17] Bao, Z., Sun, C. Y., and Xing, M. D.
Time-frequency approaches to ISAR imaging of maneuvering targets and limitations.
IEEE Transactions on Aerospace and Electronic Systems, **37**, 3 (July 2001), 1092–1099.

[18] Berizzi, F., Mese, E. D., Diani, M., and Martorella, M.
High-resolution ISAR imaging of maneuvering targets by means of the range instantaneous Doppler technique: modeling and performance analysis.
IEEE Transactions on Image Processing, **10**, 12 (Dec. 2001), 1880–1890.

[19] Li, Y. C., Wu, R., Xing, M., and Bao, Z.
Inverse synthetic aperture radar imaging of ship target with complex motion.
IET Radar, Sonar, and Navigation, **2**, 6 (Dec. 2008), 395–403.

[20] Chen, V. C., and Ling, H.
Time–Frequency Transform for Radar Imaging and Signal Analysis. Boston: Artech House, 2002.

[21] Wang, Y., Ling, H., and Chen, V. C.
ISAR motion compensation via adaptive joint time-frequency technique.
IEEE Transactions on Aerospace and Electronic Systems, **34**, 2 (1998), 670–677.

[22] Thayaparan, T., Lampropoulos, G., Wong, S. K., and Riseborough, E.
Application of adaptive time-frequency algorithm for focusing distorted ISAR images from simulated and measured radar data.
IEE Proceedings—Radar, Sonar, and Navigation, **150**, 4 (2003), 213–220.

[23] Zhu, D., Yu, X., and Zhu, Z.
Algorithms for Compressed ISAR Autofocusing.
In *Proceedings of 2011 IEEE CIE International Conference on Radar*, Chengdu, China, 533–536, Oct. 24–27, 2011.

[24] Ye, W., Yeo, T. S., and Bao, Z.
Weighted Least-Squares estimation of phase errors for SAR/ISAR autofocus.
IEEE Transactions on Geoscience and Remote Sensing, **37**, 5 (Sep 1999), 2487–2494.

[25] Berizzi, F., and Cosini, G.
Autofocusing of inverse synthetic aperture radar images using contrast optimization.
IEEE Transactions on Aerospace and Electronic Systems, **32**, 3 (Jul. 1996), 1185–1191.

[26] Martorella, M., Berizzi, F., and Haywood, B.
Contrast maximisation based technique for 2-D ISAR autofocusing.
Proceedings of the IEEE—Radar, Sonar, and Navigation, **152**, 4 (Aug. 2005), 253–262.

[27] Kragh, T. J., and Kharbouch, A. A.
Monotonic iterative algorithm for minimum-entropy autofocus.
In *Proceedings of the IEEE International Conference on Image Processing*, Atlanta, GA. 645–648, 2006.

[28] Du, X. Y., Duan, C. W., and Hu, W. D.
Sparse representation based autofocusing technique for ISAR images.
IEEE Transactions on Geoscience and Remote Sensing, **51**, 3 (Mar. 2013), 1826–1835.

[29] Onhon, N. O., and Çetin, M.
A nonquadratic regularization-based technique for joint SAR imaging and model error correction.
In *Proceedings of SPIE, Algorithms for Synthetic Aperture Radar Imagery XVI*, Orlando, FL, **7337**, 73370C, 2009.

[30] Zhang, L., Qiao, Z. J., Xing, M. D., Sheng, J. L., Guo, R., and Bao, Z.
High-resolution ISAR imaging by exploiting sparse apertures.
IEEE Transactions on Antenna and Propagation, **60**, 2 (Feb. 2012), 997–1008.

[31] Candès, E., Romberg, J., and Tao, T.
Robust uncertainty principles: exact signal reconstruction from highly incomplete frequency information.
IEEE Transactions on Information Theory, **52**, 2 (Feb. 2006), 489–509.

[32] Candès, E., Romberg, J., and Tao, T.
Near-optimal signal recovery from random projections: universal encoding strategies?
IEEE Transactions on Information Theory, B, 2 (Feb. 2006), 489–509.

[33] Donoho, D.
Compressed sensing.
IEEE Transactions on Information Theory, **52**, 4 (Apr. 2006), 5406–5425.

[34] Chen, C. C., and Andrews, H. C.
Target-motion-induced radar imaging.
IEEE Transactions on Aerospace and Electronic Systems, **AES-16**, 1 (Jan. 1980), 2–14.

[35] Wang, J., and Kasilingam, D.
Global range alignment for ISAR.
IEEE Transactions on Aerospace and Electronic Systems, **39**, 1 (Jan. 2003), 351–357.

[36] Jakowatz, C. V., Jr., and Wahl, D. E.
Eigenvector method for maximum-likelihood estimation of phase errors in synthetic-aperture-radar imagery.
Journal of the Optical Society of America, **10**, 12 (Dec. 1993), 2539–2546.

[37] Sauer, T., and Schroth, A.
Robust range alignment algorithm via Hough transform in an ISAR imaging system.
IEEE Transactions on Aerospace and Electronic Systems, **31**, 3 (Jul. 1995), 1173–1177.

[38] Chan, H. L., and Yeo, T. S.
Noniterative quality phase-gradient autofocus (QPGA) algrotihm for spotlight SAR imagery.
IEEE Transactions on Geoscience and Remote Sensing, **36**, 5 (Sep. 1998), 1531–1539.

[39] Zhang, L., Xing, M. D., Qiu, C. W., Li, J., Sheng, J., Li, Y., and Bao, Z.
Resolution Enhancement for Inversed Synthetic Aperture Radar Imaging under Low SNR via Improved Compressive Sensing.
IEEE Transactions on Geoscience and Remote Sensing, **48**, 10 (Oct. 2010), 3824–3838.

[40] Sturm, J. F.
Using SeDuMi 1.02, a Matlab toolbox for optimization over symmetric cones. Department of Econometrics, Tilburg University, Tilburg, The Netherlands, Tech Rep., August 1998–October 2001.

[41] Donoho, D. L., Driori, I., Stodden, V. C., and Tsaig, Y. SparseLab. [Online]. 2007. Available: http://sparselab.stanford.edu/.

[42] Grant, M., Boyd, S., and Ye, Y. cvx: Matlab software for disciplined convex programming. [Online]. Available: http://www.stanford.edu/˜boyd/cvx/.

[43] Zhang, Y. YALL1. [Online]. Available: http://www.caam.rice.edu/˜optimization/L1/YALL1/.

[44] Guo, X., Sun, H. B., and Wang, S. L.
Comments on discrete chirp-Fourier transform and its application to chirp rate estimation.
IEEE Transactions on Signal Processing, **50**, 12 (Dec. 2002), 3115–3116.

[45] Chen, V. C., and Qian, S.
Joint time-frequency transform for radar range-Doppler imaging.
IEEE Transactions on Aerospace and Electronic Systems, **34**, 2 (Apr. 1998), 486–499.

[46] Jones, D. L., and Baraniuk, R. G.
An adaptive optimal-kernel time-frequency representation.
IEEE Transactions on Signal Processing, **43**, 10 (Oct. 1995), 2361–2371.

[47] Doerry, A. W.
Autofocus Correction of Excessive Migration in Synthetic Aperture Radar Images. Sandia, Albuquerque, NM, Rep. SAND2004-4770, Sept. 2004.

[48] Perry, R. P., Dipietro, R. C., and Fante, R. L.
SAR imaging of moving targets.
IEEE Transactions on Aerospace and Electronic Systems, **35**, 1 (Jan. 1999), 57–66.

[49] Xing, M. D., Wu, R. B., Lan, J. Q., and Bao, Z.
Migration through resolution cell compensation in ISAR imaging.
IEEE Geoscience and Remote Sensing Letters, **1**, 2 (Apr. 2004), 141–144.

[50] Li, G., Zhang, H., Wang, X., and Xia, X.-G.
ISAR 2-D imaging of uniformly rotating targets via matching pursuit.
IEEE Transactions on Aerospace and Electronic Systems, **48**, 2 (Apr. 2012), 1838–1846.

[51] Rao, W., Li, G., Wang, X., and Xia, X.
ISAR imaging of maneuvering targets with missing data via matching pursuit.
In *Proceedings of the IEEE Radar Conference*, Kansas City, MO, May 2011, 124–128.

Lei Zhang was born in Zhejiang Province, China, in 1984. He received a B.S. degree in mechanical and electrical engineering from Chang'an University in 2006 and a doctoral degree in signal and information processing from Xidian University in 2012. He is currently working as a lecturer at the National Laboratory of Radar Signal Processing, Xidian University. His major research interests are radar imaging (SAR/ISAR) and motion compensation.

Jia Duan was born in Jiangxi Province, China, in 1989. She is currently working toward a Ph.D. degree at the National Laboratory of Radar Signal Processing, Xidian University. Her major research interest is ISAR imaging.

Zhijun Qiao (M'10) received a Ph.D. degree in applied math from the Institute of Mathematics, Fudan University, Shanghai, China, in 1997, where his dissertation was one of the first 100 excellent Ph.D. dissertations awarded in 1999. From 1999 to 2001, he was a Humboldt Research Fellow with the Department of Mathematics and Computer Science, University of Kassel, Germany. From 2001 to 2004, he was a Researcher with the Theoretical Division, Los Alamos National Laboratory. He was also a Professor with the Department of Mathematics, Liaoning University, Shenyang City, China, since 1997. Currently, he is the principal investigator of two grants under the Department of Defense program and the Norman Hackerman Advanced Research Program. He is currently with the Department of Mathematics, The University of Texas-Pan American, in Edinburg, TX. His research interest includes nonlinear partial differential equations and its application in radar imaging.

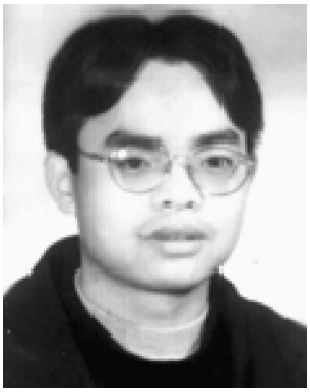

Mengdao Xing (M'04) was born in Zhejiang, China, in November 1975. He received a bachelor's degree and a Ph.D. degree in 1997 and 2002, respectively, from Xidian University, both in electrical engineering. He is currently a full professor with the National Key Laboratory for Radar Signal Processing, Xidian University. His research interests include SAR, ISAR, and over-the-horizon radar (OTHR).

Zheng Bao (M'80—SM'90) was born in Jiangsu, China. Currently, he is a professor with Xidian University and the chairman of the academic board of the National Key Laboratory of Radar Signal Processing. He has authored or coauthored six books and published more than 300 papers. Now, his research fields include space-time adaptive processing (STAP), radar imaging (SAR/ISAR), automatic target recognition (ATR), and over-the-horizon radar (OTHR) signal processing. Professor Bao is a member of the Chinese Academy of Sciences.